

# Spherulitic Crystal Growth Drives Mineral Deposition Patterns in Collagen-Based Materials

Elena Macías-Sánchez,\* Nadezda V. Tarakina, Danail Ivanov, Stéphane Blouin, Andrea M. Berzlanovich, and Peter Fratzl\*

The formation of the hard tissues that provide support and mobility to organisms is achieved through the interplay of inorganic crystals and an organic framework composed of collagen and a small percentage of non-collagenous proteins. Despite their clinical relevance, the mechanisms governing mineralization of the extracellular matrix are still poorly understood. By using 3D electron tomography and high-resolution electron microscopy imaging and spectroscopy, it has been demonstrated that mineralization proceeds through a spherulitic-like crystal growth process. First, aggregates of disordered crystals form in the interfibrillar spaces, which lead to the mineralization of adjacent fibrils. Mineral propagates steadily through the inter- and intrafibrillar spaces of the collagen structure forming layered spherulites that grow to confluence. The structure of the collagen fibrils serves as a protein scaffold to guide the formation of a myriad of platelet-shaped crystallites that make up each of these spherulites. At their periphery, nanosized unmineralized areas remain, leading to the formation of the characteristic lacy pattern observed in the transversal cross-section of mature calcified tissues. This study provides fundamental insights into the bone formation process and represents a potential strategy for complex materials design.

organism. Its outstanding mechanical properties arise from a delicate balance of nanoscale interactions between type I collagen fibrils, hydroxyapatite crystals, and regulatory molecules such as non-collagenous proteins (NCPs) and proteoglycans (PGs). Collagen fibrils provide the structural scaffold for the mineral to grow, and NCPs and PGs help guide the assembly and mineralization of the collagen fibrils.<sup>[1]</sup>

Although much progress has been made in understanding bone structure at nanoscale in recent decades, there remains a knowledge gap between the early stages of mineralization and the formation of the final mineral deposition pattern. It is generally accepted that early mineralization initiates with the formation of mineral spherulites, having been documented in numerous tissues, such as embryonic chick tibia,<sup>[2–6]</sup> embryonic rat alveolar bone,<sup>[6,7]</sup> and turkey leg tendon.<sup>[8–12]</sup> Several terms, such as mineral foci, spherulites, clusters or aggregates


have been used to define the calcium phosphate-containing spherical bodies occurring in the osteoid in the vicinity of the osteoblasts.<sup>[2,6]</sup> They appear in the interfibrillar spaces, often forming linear arrangements, and propagate within the fibrils,<sup>[12]</sup> leaving a zone free of mineral around the canaliculi

## 1. Introduction

Bone is a complex hierarchical nanocomposite with an extraordinary combination of stiffness and toughness, perfectly adapted to provide mechanical support and protection to our

E. Macías-Sánchez  
Department of Biochemistry  
Radboud Institute for Molecular Life Sciences  
Radboud University Medical Center  
Geert Grooteplein Zuid 28, 6525 GA Nijmegen, Netherlands  
E-mail: elena.macias@radboudumc.nl

E. Macías-Sánchez, P. Fratzl  
Department of Biomaterials  
Max Planck Institute of Colloids and Interfaces  
Am Mühlenberg 1, 14476 Potsdam, Germany  
E-mail: fratzl@mpikg.mpg.de

 The ORCID identification number(s) for the author(s) of this article can be found under <https://doi.org/10.1002/adfm.202200504>.

© 2022 The Authors. Advanced Functional Materials published by Wiley-VCH GmbH. This is an open access article under the terms of the Creative Commons Attribution-NonCommercial License, which permits use, distribution and reproduction in any medium, provided the original work is properly cited and is not used for commercial purposes.

N. V. Tarakina  
Department of Colloid Chemistry  
Max Planck Institute of Colloids and Interfaces  
Am Mühlenberg 1, 14476 Potsdam, Germany

D. Ivanov  
Department of Inorganic Chemistry  
Fritz Haber Institute of the Max Planck Society  
Faradayweg 4–6, 14195 Berlin, Germany

S. Blouin  
Ludwig Boltzmann Institute of Osteology  
Hanusch Hospital of OEGK and AUVVA Trauma Centre Meidling  
1st Medical Department Hanusch Hospital, Kundratstraße 37  
1120 Vienna, Austria

A. M. Berzlanovich  
Unit of Forensic Gerontology  
Center of Forensic Science  
Medical University of Vienna  
Spitalgasse 23, 1090 Vienna, Austria

DOI: 10.1002/adfm.202200504

and Haversian canal.<sup>[13]</sup> Only recently it has been proposed that these spherulites give rise to micrometer-sized mineral ellipsoids that imbricate forming a new hierarchical level of organization in bone<sup>[14,15]</sup> also called tessellation.<sup>[15]</sup> However, due to the limited resolution of the studies performed so far, it is still unknown how these aggregates grow and how mineralization progresses through the extracellular matrix (ECM) and results in the mature mineral deposition pattern.

The 3D mineral ultrastructure of bone has puzzled researchers for decades, as the patterns observed in the different projections (parallel and perpendicular to the collagen fibrils) are completely dissimilar. The longitudinal cross-section shows the characteristic banding pattern of the collagen fibrils, enhanced by preferential mineral deposition within the gap zones (filamentous pattern). In contrast, circular patterns are observed in transversal cross-section, which interestingly include nonmineralized areas surrounded by curved and thin mineral particles (lacy pattern).<sup>[16–18]</sup> We now know that filamentous and lacy patterns form a single 3D mineral network,<sup>[17,18]</sup> but there are still many unanswered questions related to the formation of this 3D structure, for example why and how these nonmineralized areas appear in transversal cross-section. Additionally, it was recently proposed that the mineral forms a continuous cross-fibrillar phase that surpasses the typical dimensions of a single collagen fibril.<sup>[18,19]</sup> However, the simultaneous identification of the organic and mineral phase at electron microscopic resolution remains elusive.

Decoding the structural relationships of the organic and inorganic phases at the nanoscale is crucial, because of its profound implications on the mechanical performance of mineralized tissues. Impaired mineralization is the main clinical feature of several bone disorders. However, the mechanistic understanding of the mineralization process remains largely incomplete. A deeper comprehension of the processes governing the propagation of the mineral phase through the organic ECM would advance our understanding not only of bone formation, but also of regenerative and pathological processes involving new matrix deposition, as well as provide new directions for the design of biomimetic materials.

Using transmission electron microscopy combined with focused ion beam scanning electron microscopy, we have studied the early stages of mineralization using a model system for mineralizing collagen, the turkey tendon. Avian tendon calcification becomes active as the animal ages and gradually progresses along the collagen direction. The possibility to identify the mineralization front and to monitor the mineralization process has made this model one of the most widely used for mineralization studies.<sup>[8,9,12]</sup> The main difference with other bone types is its simplified structure of parallel collagen fibrils, similar to parallel fibered bone, and a higher proportion of completely unmineralized collagen fibrils. This fact permits a relatively simple identification of collagen fibrils and their interaction with early mineral deposits, compared to the bone where the collagen arrangement is more complex.<sup>[13]</sup>

We demonstrate that the final 3D mineral ultrastructural pattern arises from the formation and confluence of spherulitic mineral clusters that grow along and across the collagen fibrils, encompassing inter- and intrafibrillar spaces. These spherulites are composed of a multitude of mineral platelets allocated

along curved layers within the fibrils. Nanosized spaces remain unmineralized within the collagen fibril, giving rise to the characteristic lacy pattern observed in transversal cross-section. Finally, we demonstrate that the same ultrastructural pattern is found in different types of bone, providing compelling evidence that the mechanism of mineralization is homologous in different tissues.

## 2. Results and Discussion

### 2.1. 3D Mineral Structure Arises from the Formation and Growth of Mineral Spherulites

To resolve the mechanism by which the mineral propagates through the ECM, we performed a correlative study over multiple length scales, coupling Environmental Scanning Electron Microscopy (ESEM), Focused Ion Beam-Scanning Electron Microscopy (FIB-SEM) 3D imaging, FIB lamella preparation and ultramicrotomy for Scanning/Transmission Electron Microscopy (S/TEM) and STEM-EDS (Energy Dispersive X-ray Spectroscopy). Just after slaughter, the tendon was prepared by high-pressure freezing and freeze substitution, maintaining the native structure and composition of the ECM (see “Experimental Section” for details).

Avian tendons (**Figure 1**, transversal cross-sections) are composed of a simplified structure of parallel collagen fibrils, where tendon fibroblasts and cell processes surround and define the fibril bundle structural unit (**Figure 1a**). Mineralization commences from a mid-way point along the tendon and proceeds proximally into the muscle (**Figure S1**, Supporting Information). At the mineralization front, nanosized mineral foci appeared mainly in the vicinity of the cell processes (**Figure 1b**), with a diameter ranging between 50–150 nm, in line with sizes reported in other systems, both *in vivo* and *in vitro*.<sup>[2,20]</sup> With a higher mineral content, these spherulites became larger in diameter and spread across the fibrils (**Figure 1c**), coalescing until the complete mineralization of the fibril bundle (**Figure 1d**). The fibril bundle is surrounded by cell processes and a collagen layer arranged perpendicular to the fibrils in the bundle<sup>[12,21]</sup> that also mineralizes over time (**Figure 1d**). This structure appears to delimit the growth of spherulites, as they never appear transversely across the bundles.

Spherulites displayed a nearly circular profile in transversal cross-section (0.7–2.5  $\mu\text{m}$  in diameter) (**Figure 1e,f**), and elongated several microns (2–3  $\mu\text{m}$  in length) along the collagen fibrils, in the shape of prolate spheroids (**Figure 1g,h**), in line with previous reports.<sup>[12,14,15]</sup> Although in transversal cross-section the spherulites appear to be constituted of needle-like grains radiating from the central area (**Figure 1e,f**), the 3D reconstruction of the FIB-SEM data revealed that they are indeed layers: they are connected in the third dimension (**Figure 1g,h**).

### 2.2. Lacy Pattern Results from the Confluence of Mineral Spherulites

In order to discard possible alterations in crystal arrangement and orientation caused by mechanical stress during ultramicrotome

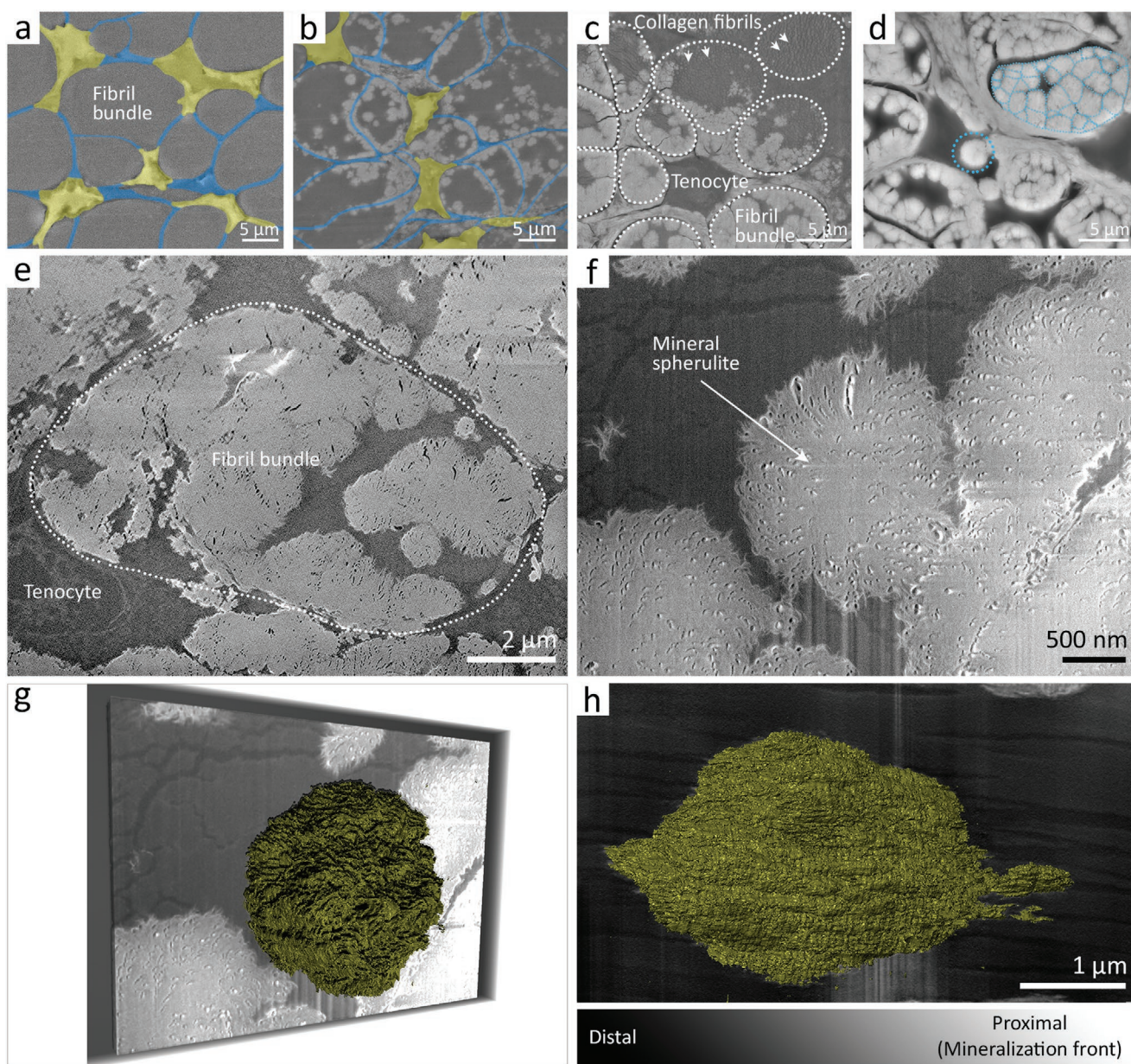


**Figure 1.** Mineralization through the formation of mineral spherulites. a) Cell network in a nonmineralized area formed by tendon fibroblasts (yellow) connected through cell processes (blue). Fibril bundles are defined by the cell processes. b) Early mineral spherulites (high contrast, brighter) at the mineralization front mainly associated with cell processes (blue). c) Propagation of minerals through the bundles (marked with dotted lines). Arrows indicate collagen fibrils. d) Mineral spherulites grow to impingement (blue dotted lines), resulting in complete mineralization of the bundle [a–d] ESEM back-scattered images]. e) FIB-SEM backscatter image of osmium and uranyl acetate-stained region of mineralizing avian tendon. Contrast is achieved due to the differential staining of the cellular (tenocytes) components and differences in atomic number (mineral spherulites). f) FIB-SEM backscatter image from the dataset (800 images) used for reconstruction. g) 3D reconstruction (lateral view) evidences the curved layers at the surface of the spherulite. h) 3D reconstruction (longitudinal view) shows a prolate spheroidal shape. All images (except h) are transversal cross-sections.

sectioning, FIB-lamellae were prepared by in situ lift-out (Figure 2). FIB lamellae present an entirely even surface that makes them ideal for elemental analysis (EDS mapping).

In addition, the thinness of the FIB-lamellae allows for a higher resolution, revealing the internal structure of the mineral spherulites (Figure 2a), which in transversal cross-section comprises a densely mineralized center composed of nonpreferentially oriented crystals (Figure 2b, Selected

Area Electron Diffraction (SAED)) that evolves into a layered structure (Figure 2b,c). In some cases, an organic core may appear (see Figure 2d, and EDS data Figure 2e,f). These areas of disordered crystalline growth are likely to be formed in the interfibrillar spaces (Figure 2g, arrowheads). Although interfibrillar mineralization has received much less attention in the literature, there are some observations that indicate that the mineral is randomly arranged in the interfibrillar spaces.<sup>[22]</sup>

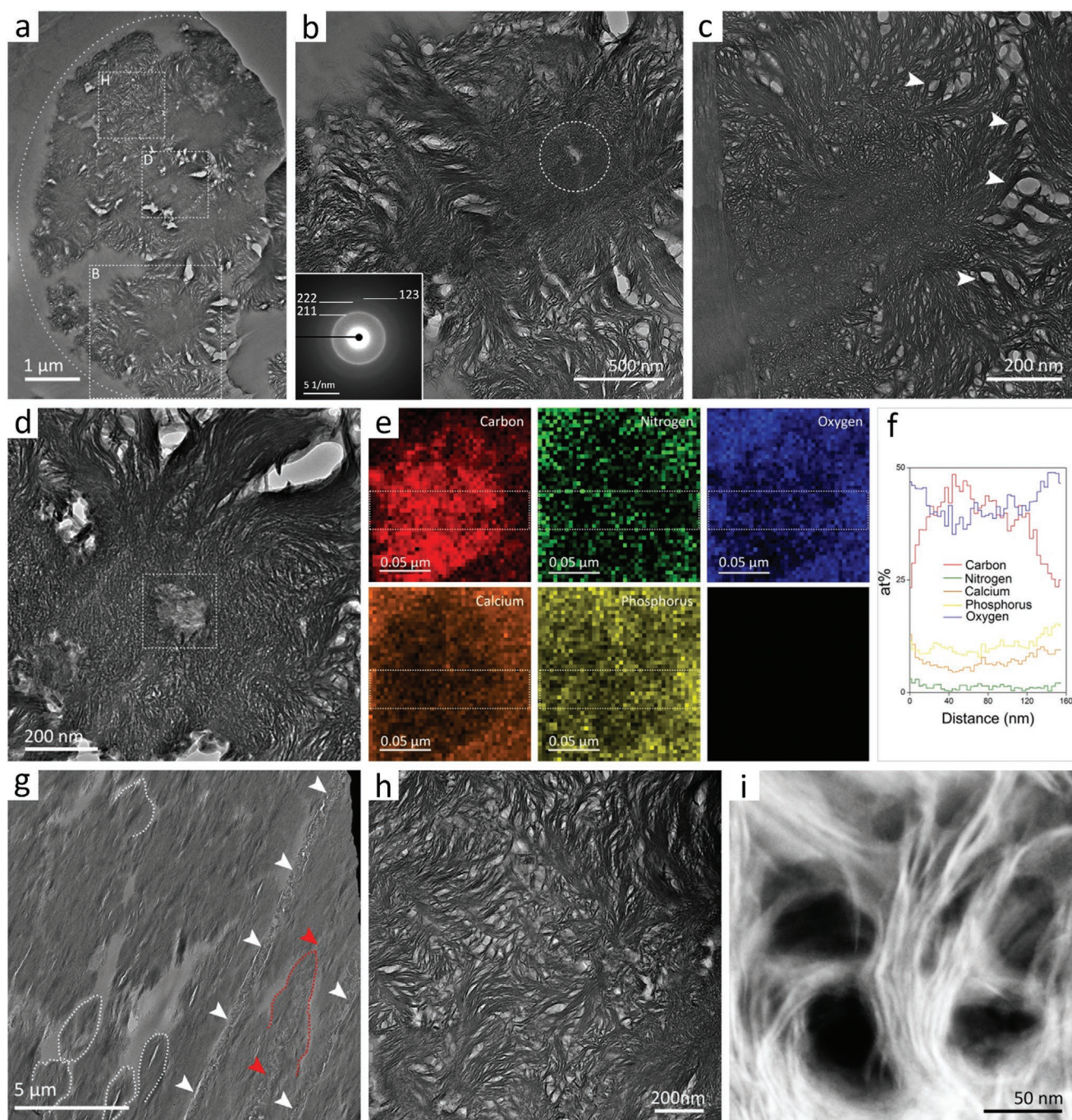


**Figure 2.** Spherulites grow to impingement, resulting in the lacy pattern. a) FIB lamella taken from the mineralization front displays a high density of mineral spherulites. The dotted line indicates the fibril bundle. Dotted boxes designate areas shown in b, d and h. b) The denser center is formed by nonpreferentially oriented crystals (see SAED) from where serpentine layers emerge. The dotted circle indicates the electron diffraction area. c) Nonmineralized lentil-shaped spaces (arrowheads) are found between the layers. d) Spherulite showing a central area enriched in organic material. e) EDS maps of the organically enriched core (area framed in d). f) Atomic ratio (at%) extracted from the area of the maps surrounded by the dotted box. g) Longitudinal cross-section of a highly mineralized (26 weeks) turkey leg tendon. Interfibrillar mineralized spaces (arrowheads) running parallel to the collagen fibrils are visible. In areas where the mineralization is still incomplete, the oval profiles of some mineral spherulites are still recognizable (dotted lines). The spherulite indicated by the red dotted line and arrowheads displays a disorganized mineral center which corresponds to interfibrillar mineralization. h) The characteristic lacy pattern is evident where the spherulites meet. i) Detail of nonmineralized areas of the lacy pattern. [a–d, g–h] BF TEM images; i) ADF STEM image].

Longitudinal cross-sections show that these spaces mineralize in an inhomogeneous way, showing an organo-mineral patchy structure (Figure S2, Supporting Information), which

is likely the result of the high content of NCPs and PGs surrounding the fibrils. Such an internal structure containing an organic core (Figure 2g, in red) suggests that crystallization

was triggered in the interfibrillar spaces, likely by the interaction with macromolecular aggregates, expanding later into the collagen fibrils.

Propagation of the mineral phase through the collagen fibrils results in a layered structure (Figure 2b,c). A multitude of serpentine nonbranched layers emerge radially (Figure 2b–d), leaving elongated spaces devoid of minerals between them: the characteristic lentil-shaped nonmineralized areas of the so-called lacy pattern (Figure 2c, arrowheads). Enlarged views from the area where two spherulites meet show clearly the pattern (Figure 2h,i), demonstrating that it is therefore the result of a spherulitic growth process.

Among the different terms used in the literature, “spherulite” is the one that best describes the crystalline growth process. The term “spherulite” gathers polycrystalline growth patterns that arise from nonequilibrium processes, and has been used to designate a variety of morphologies.<sup>[23]</sup> Although the described mineral structures may differ from conventional spherulites in some aspects (e.g., the presence of disordered crystalline core) we think they comply with the fundamental aspects that define the spherulitic growth: space-filling tendency, polycrystallinity,

and elongated fiber-like and/or layered grains radially arranged about a center.<sup>[24]</sup> The formation of spherulites in calcium phosphate synthetic systems is well-documented.<sup>[19,25]</sup> Fluorapatite spherulite formation in gelatin medium has been intensely studied by Kniep and coworkers,<sup>[26]</sup> and other examples have been found associated with protein-mediated mineralization processes.<sup>[27]</sup>

### 2.3. Spherulites Contain Multitude of Mineral Platelets

To further study the internal structure of the spherulite, we have made use of the unique topographic information provided by the ultramicrotome slices. Sectioning of brittle materials such as minerals and ceramics (hardness  $\geq 500$  MPa) involves microcrack initiation and propagation.<sup>[28]</sup> The knife initiates a crack, which follows the path of the weakest molecular strength,<sup>[29]</sup> generating a microfracture surface. The surface topography of the ultramicrotomy slices can nowadays be visualized thanks to the presence of Secondary Electron (SE) detectors in state-of-the-art TEM microscopes.

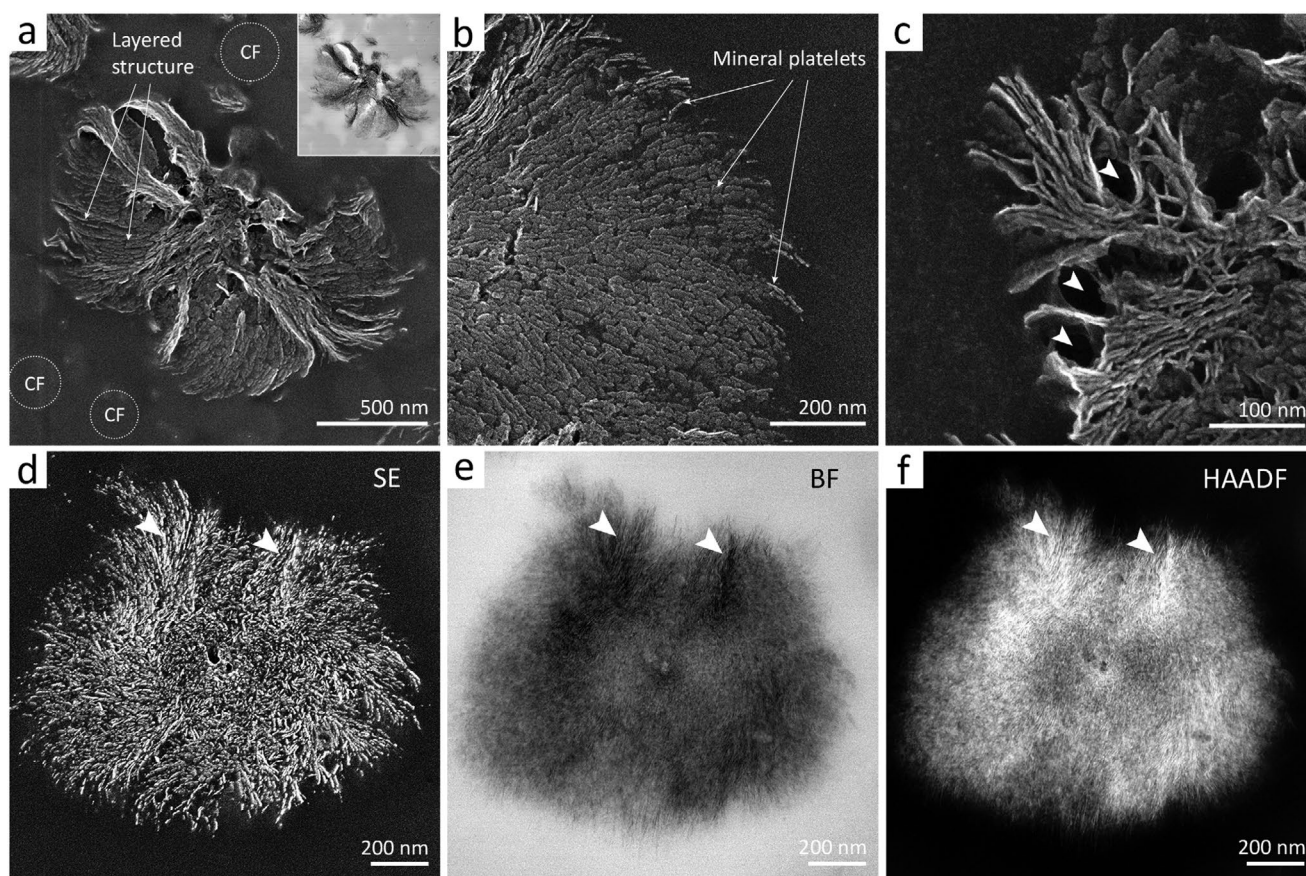


**Figure 3.** Spherulites internal layered structure accommodates a multitude of crystal platelets. a) Topographic (SE) and Bright Field (BF) (inset) Scanning Transmission Electron Microscopy (STEM) images of a mineral spherulite. Overlapping layers of crystal aggregates radiate from the center. CF: collagen fibril. b) Topographic (SE) STEM image from the periphery of a spherulite evidence the crystal aggregates that make up each layer. c) Nonmineralized circular areas appearing at the periphery of the spherulites (arrowheads) observed by secondary electrons. Bigger platelets are found in some areas as a result of the aggregation process. d–f) Simultaneous acquisition by different STEM imaging techniques of an early spherulite: Secondary Electron (SE), Bright Field (BF), and High Angle Annular Dark Field (HAADF). Crystallites arranged in layers (d) and superimposed along the thickness of the sample may appear as long, individual crystals in transmitted images (BF and HAADF) at moderated magnifications (arrowheads).

Topographic (SE) imaging (Figure 3; see also Figure S3, Supporting Information) revealed that the spherulites consist of a myriad of platelet-shaped crystals, with thickness in the order of 3–8 nm, in agreement with previous reports.<sup>[9,30]</sup> To our knowledge, SE images of the mineral platelets are available for the first time. Layers evidence a pronounced curvature (Figure 3a,b), likely determined by the internal structure and twisting of the fibrils.<sup>[31]</sup> The interlayer spacing is in the range of 3–6 nm, in line with the dimensions of the collagen microfibril unit cell ( $a = 3.9$  nm,  $b = 2.7$  nm,  $c = 67.8$  nm).<sup>[32]</sup> Greater variability in the shape and arrangement of the platelets has been found in the outer zones of the spherulites, where non-mineralized areas appear (Figure 3c).

References to “curved crystals” in the context of the lacy pattern have been abundant.<sup>[16–18,33–35]</sup> They have been described to be  $\approx 100$  nm in length,<sup>[18]</sup> and with an average radius of curvature of  $20 \pm 4$  nm.<sup>[34]</sup> Other examples have been observed in the early mineralization of bone collagen fibrils.<sup>[36,37]</sup> However, our data show that these “curved crystals” are layers containing a multitude of irregularly shaped platelets (compare Figure 2b–d and Figure 3; Figure S3, Supporting Information). Two different aspects have to be considered here. Superposition of crystallites arranged in layers throughout the thickness of the sample may appear as long, individual crystals in transmission images (Figure 3a, inset; Figure 3d–f; Figure S4, Supporting Information). In addition, a platelet aggregation process is known to occur,<sup>[38]</sup> and curved crystalline aggregates may result from the fusion of platelets allocated to the same layer.

## 2.4. Mineralization Spans Intra- and Interfibrillar Spaces

The nature of the nonmineralized spaces found in the lacy pattern has been the subject of extensive debate. Several studies have identified them with collagen fibrils,<sup>[16,17,33–35]</sup> although their shape and size do not entirely correspond.<sup>[18]</sup> It is important to note that the high mineral density in fully mineralized bone (as used in previous studies) did not allow visual or chemical identification of the collagen fibrils,<sup>[16–18,33–35]</sup> so conclusive evidence is still lacking. The great advantage of our model system is that the mineralization is not complete, allowing a clear identification of the collagen fibrils (200–300 nm diameter in this study). However, this fact introduces further complexity during sample preparation, as mineralized and nonmineralized areas may respond differently throughout the preparation process, so we cannot rule out minor displacements between fibrils.

Nonmineralized areas (30–60 nm) visible within the spherulites (Figure 4a–c), were clearly smaller than the collagen fibrils. Additionally, we used elemental mapping to unambiguously locate the organic and inorganic components. The integrity of the surface of the FIB-lamella was checked by SE imaging (Figure S5, Supporting Information), ruling out the possibility of damaged areas (i.e., holes) and verifying that no surface topography influences EDS mapping. Unmineralized collagen fibrils retrieved intense nitrogen signal, hallmark of proteins. Calcium, phosphorous and oxygen co-localized with the collagen fibrils (nitrogen), demonstrating intrafibrillar mineralization (see Figure 4d, overlaid). Moreover, EDS mapping demonstrated the presence of nonmineralized areas (Figure 4c)

within the collagen fibril (Figure 4d). These areas, deficient in calcium and phosphorous, are enriched in carbon, suggesting the presence of macromolecular complexes immersed in the collagen fibril. Molecules up to 50 kDa could diffuse within the collagen fibril and impact collagen mineralization.<sup>[39]</sup> Indeed, small molecules such as osteocalcin (5.7 kDa) and osteonectin (40 kDa) have been immunolocalized within the collagen fibril in the turkey tendon<sup>[22]</sup> and in calf scapula bone<sup>[40]</sup> respectively. Although the function of these molecules is still controversial, it seems to be clear that they act as mineralization regulators.

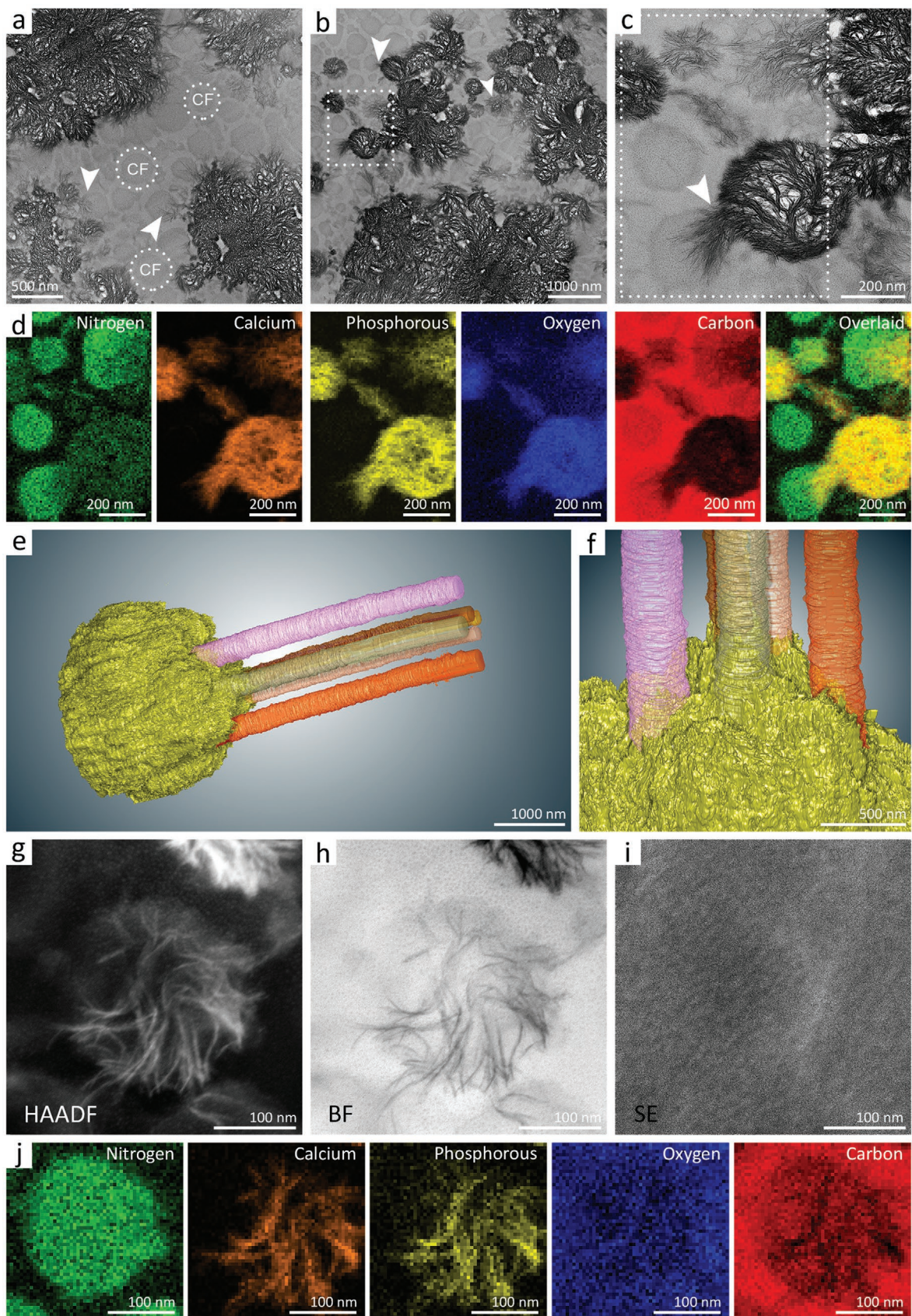
Even more importantly, our data demonstrate that the mineral permeates the collagen fibrils, spreading from one fibril to the adjacent ones and across the interfibrillar spaces (Figure 4a–c, arrowheads; Figure 4e,f). The extent to which intra- or inter-fibrillar mineralization prevails in the collagen macroarchitecture has been largely debated because of its deep implications in the mechanical performance of calcified tissues and biomechanical modeling.<sup>[41]</sup> Here we provide consistent evidence, combining imaging, chemical analysis, and FIB-SEM 3D reconstruction (Figure 4a–f), demonstrating that the propagation of mineralization through the collagen macroarchitecture surpasses the physical limit of a single collagen fibril, connecting intra- and interfibrillar mineralization. This argument was formally suggested,<sup>[18,19]</sup> but not yet proven.

In addition, we provide higher magnification images showing crystal layers with marked curvature within an individual collagen fibril (intrafibrillar mineralization) (Figure 4g–j). Similar examples have been shown in the early mineralization of bone collagen fibrils from embryonic chicken skulls<sup>[36]</sup> and herring (*Americanus americanus*) bone.<sup>[37]</sup> In this case, the addition of chemical imaging (Figure 4j, EDS mapping), allows them to be unambiguously identified, and reveals the complexity of the path that these layers can follow within an individual collagen fibril.

## 2.5. Homologous Mineralization Mechanism of Bone Tissues

To evaluate the validity of our results and their relevance to bone, samples from bovine and human femur were prepared by ion-polishing (see “Experimental Section” for details). Highly mineralized distal tendon regions, bovine femur (fibrolamellar bone), and human femur (cortical bone) showed a remarkably similar pattern in transversal cross-section (Figure 5). Higher density regions surrounded by nonmineralized areas are reminiscent of the spherulite-mediated mineralization process (Figure 5a,c,e). Because of their appearance in transversal cross-section, terms such as “rosettes”<sup>[34]</sup> have been used in the literature. These spherulites are yet visible in highly mineralized tissues even at moderate magnification, especially when the collagen fibrils are arranged perpendicular to the image plane (ESEM images, Figure S6, Supporting Information). The lacy pattern, originating from the confluence of spherulites, was evident in all bone structures (Figure 5b,d,f).

This line of evidence indicates that the lacy pattern observed in transversal cross-section is a common ultrastructural mineral deposition pattern in type I collagen-based materials, derived from an analogous mineralization mechanism based on the formation and growth of mineral spherulites. The fact that the pattern has been described in a variety of bone-like



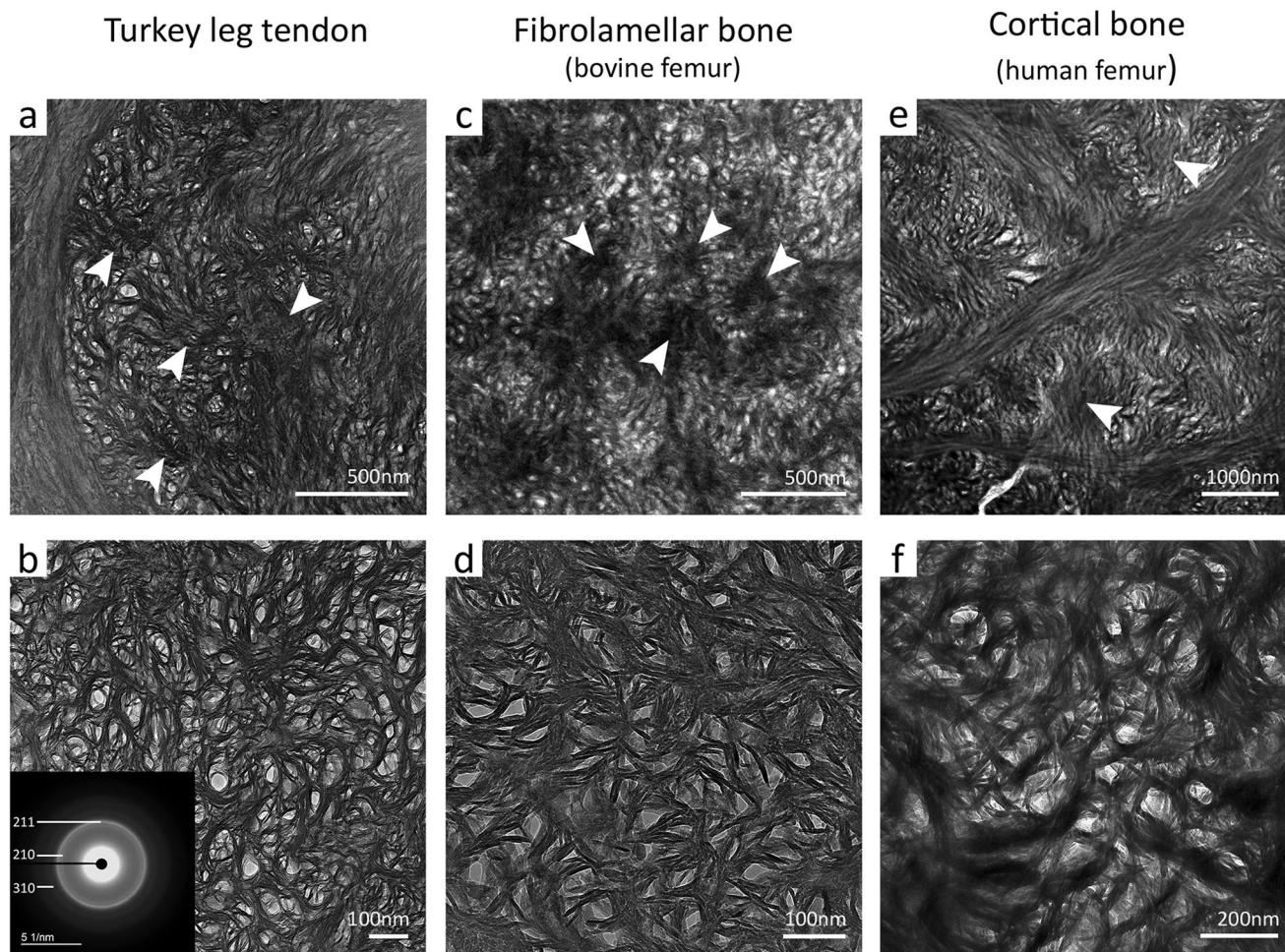


**Figure 5.** Common mineral deposition mechanism in type I collagen materials. a, c, e) Dense patches of nonpreferentially oriented mineral particles (arrowheads) surrounded by nonmineralized areas are reminiscent of the mineralization through the formation of spherulites. b, d, f) Evidence of the presence of the lacy pattern in different bone-like materials. a, b) Turkey leg tendon (FIB-lamella). c, d) Bovine femur (ion polished cross-section). e, f) Human femur (ion polished cross-section). All are Bright Field (BF) images.

materials (human cortical<sup>[17,18,42]</sup> and trabecular bone,<sup>[43]</sup> ivory dentine,<sup>[16]</sup> human dentine,<sup>[44]</sup> and bovine fibrolamellar bone<sup>[17]</sup>), suggests that there is a high degree of homology in the way these materials mineralize.

## 2.6. Further Implications: Toward a Model for the Mineralization of Type I Collagen-Based Materials

A large body of evidence now supports the idea that mineralization of collagen fibrils takes place in the presence of a highly

hydrated liquid-phase precursor induced or stabilized by NCPs (PILP process, polymer/peptide-induced liquid precursor). The amorphous mineral phase is believed to be shaped by the collagen prior to crystallization. Finally, upon dehydration, the transformation from amorphous to crystalline phase is triggered.

Experiments conducted by the Gower's lab demonstrated that, by using a polyanionic polymer to mimic the role of NCPs in stabilizing the amorphous phase, characteristic crystallographic orientation of bone can be recreated *in vitro*.<sup>[19]</sup> Interestingly, they showed how overgrown mineral particles protruding from the fibrils take on a spherulite-like shape.

**Figure 4.** Mineralization encompasses inter- and intrafibrillar spaces. a, b) Mineral spreads through the ECM from one fibril to the adjacent ones (arrowheads). Nanosized nonmineralized areas are already visible in the spherulites. Collagen fibrils (CF, dotted circles) profiles are highlighted by osmium tetroxide and uranyl acetate staining (BF TEM). c) Enlarged image of the area marked in (b). Mineral particles (lower contrast, darker) within a collagen fibril, where nonmineralized spaces (higher contrast, brighter) are evident. Edges of the collagen fibrils are visible (BF STEM). d) EDS maps (atomic ratio, at%) of the area framed in (c). Mineral locates within the fibrils and propagates to adjacent ones. Nonmineralized areas are carbon enriched. Overlapping EDS maps of N (green), Ca (orange) and, P (yellow). e) FIB-SEM reconstruction of a mineral spherulite showing how the mineral phase permeates several collagen fibrils. f) Detail of the image in (e) demonstrating a continuous mineral phase spanning inter- and intrafibrillar spaces (cross-fibrillar mineralization). g–i) Simultaneous acquisition (High Angle Annular Dark Field (HAADF), Bright Field (BF) and, Secondary Electron (SE) detectors) of the incipient mineralization of a collagen fibril. In the HAADF and BF images, markedly curved crystal layers are visible with inverse contrast. The SE image shows no defects on the sample surface. j) Semi-quantitative EDS maps demonstrate that the curved layers are located within an individual collagen fibril, clearly identified by the nitrogen signature.



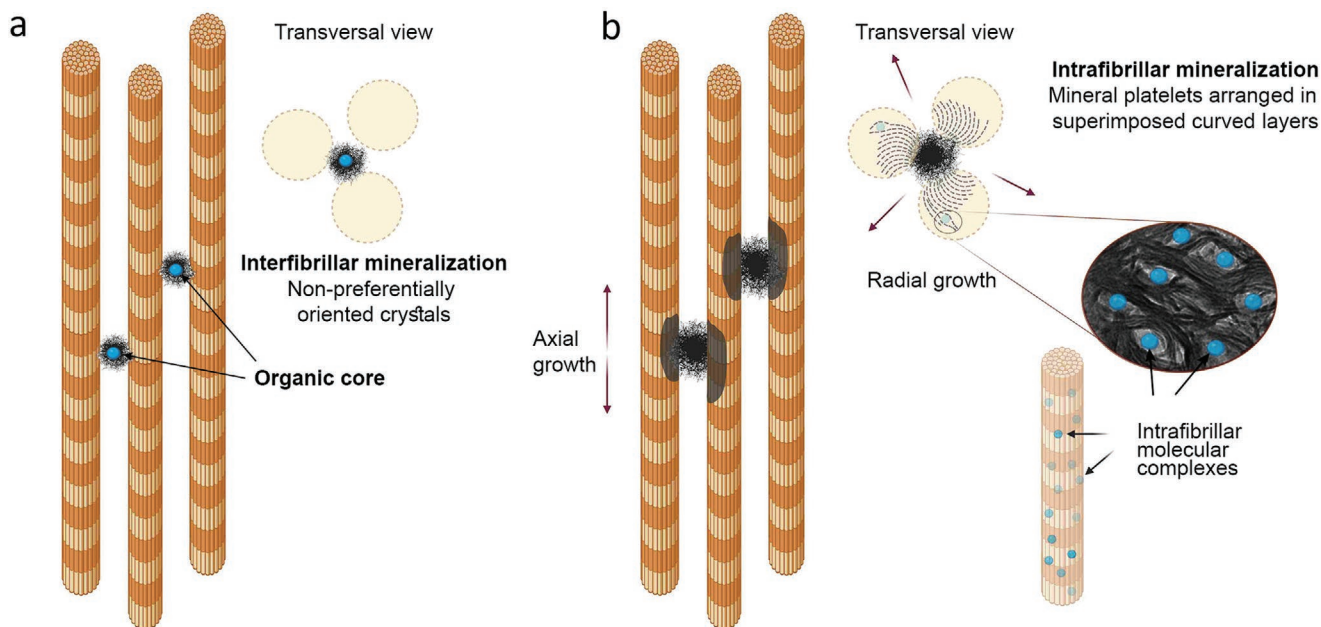


**Figure 6.** Collagen mineralization model. a) Early formation of nonoriented mineral particles in the interfibrillar spaces, which subsequently propagates through the fibril. b) Mineral crystals acquire an ordered layered arrangement provided by the collagen scaffold. The presence of macromolecular complexes (blue spheres) impacts the arrangement of the layers of crystals within the fibrils, giving rise to nonmineralized areas. Two growth directions are identified: 1) Axial growth along the ordered structure of the collagen fibril, which seems to be the fastest, as the spherulites are prolate spheroids in shape<sup>[12]</sup>; likely determined by the preferential crystallographic growth of hydroxyapatite along [001] direction. 2) Radial growth, where mineral permeates from one fibril to the adjacent ones, across the interfibrillar spaces. (Figure created with BioRender.com).

Other examples of the application of the PILP process include the formation of hydroxyapatite spherulites similar to those found in the Randall's plaque.<sup>[25]</sup> While this evidence supports the idea that the spherulitic growth could be promoted by an amorphous precursor phase, it should be also noted that a large body of literature indicates it is the result of classical ion-by-ion crystal growth (secondary nucleation at the crystal growth front).<sup>[24]</sup>

Although currently is not possible to determine the exact sequence of events of the phase transformation, the internal structure of spherulites indicates that crystallization initiates in the interfibrillar spaces (Figure 6a), from where the crystallinity percolates the adjacent collagen fibrils. Ion accretion, condensation, and stabilization of amorphous calcium phosphate (ACP) may be promoted by the presence of macromolecular complexes, such as phosphoproteins or glycosaminoglycans. In fact, bone sialoprotein<sup>[45]</sup> and keratan sulfate<sup>[46]</sup> have been immunolocalized in early mineral spherulites. The role of osteopontin<sup>[15]</sup> has also been discussed, as well as the potential role of chondrocyte membrane nanofragments in the formation of spherulites during endochondral ossification.<sup>[47]</sup>

While the crystallites found in the inter-fibrillar spaces do not present a preferential arrangement, those located along the collagen fibrils are arranged in curved superimposed layers (Figure 6b). The fact that the layers are curved (Figure 3; Figure S3, Supporting Information) implies that there are changes in the orientation of *a*- and *b*-crystallographic axes of the mineral platelets, which would therefore only be coarsely uniaxially co-oriented along the *c*-axis.<sup>[19,48]</sup> Abrupt orientation

changes have been observed within individual collagen fibrils at early stages of mineralization (Figure 4g–j), as well as in the outer zones of the spherulites, where crystal layers are more loosely and disorderly arranged, and unmineralized spaces abound (Figure 3c). However, these orientation changes appear to be gradual in the middle zones of the spherulites, where layers are well packed and ordered with respect to each other (Figure 3b; Figure S3, Supporting Information), locally resembling a stack of cards.<sup>[49]</sup> This variability seems to indicate that we are dealing with a more complex crystal arrangement than described so far, where the degree of crystal (mis)alignment correlates to some extent with the location of the crystals within the spherulite, and it is probably determined by the composition of the ECM.

We propose that the presence of macromolecular complexes (Figure 6b, blue spheres) guides crystal growth generating non-mineralized spaces. Their presence would imply a spatial hindrance leading to the deviation in the trajectory of the crystal layers. Note that the layers do not stop growing in these areas, but concentrically surround the nonmineralized spaces. Whether or not the structure of the collagen fibril is affected in these zones, and whether or not these macromolecules have crystal growth inhibitory capacity, should be explored in future studies.

### 3. Conclusion

Our study aims to fill the knowledge gap between the early stages of mineralization and the formation of mature mineral patterns in collagen-based materials. By providing simultaneous 2D and 3D identification of collagen fibrils and mineral phase,

we demonstrate that the lacy pattern observed in transversal cross-section arises from the confluence of mineral spherulites that grow in a cross-fibrillar process, encompassing inter- and intrafibrillar spaces. These mineral spherulites, which grow following the protein scaffold provided by the collagen fibrils, have a curved-layered structure that harbors a vast number of mineral platelets. The organic core presented by these spherulites could promote the initial crystalline growth. Nonmineralized spaces located within the collagen fibrils are abundant at the periphery of the spherulites, and seem to be related to the presence of macromolecules. Finally, by comparing the ultrastructure of different bone types, we suggest a homologous mechanism operating in different type I collagen-based materials.

This protein-mediated mineralization process seems to be tightly controlled, where the ECM acts as a functionalized matrix where the distribution of macromolecular complexes may trigger the formation of mineral spherulites of regular shape and size. We anticipate that the incorporation of these principles will change our understanding of the bone formation, providing potential new avenues for applications in the design and engineering of hard tissue repair and regeneration.

## 4. Experimental Section

**Sample Collection:** Legs from 15 weeks-old common turkey (*Meleagris gallopavo*) were collected from a local farm (Putenhof Bornum, Bockenem, Germany) immediately after slaughter and transported in minced ice. Once at the lab, *Gastrocnemius* tendon was carefully dissected by means of a surgical scalpel, scraping off the remains of adjacent tissue. Rectangular sections ( $\approx 500 \times 300 \mu\text{m}$ ) were cut under a binocular microscope from the mineralization front area (proximal part, close to the muscle; Figure S1, Supporting Information) along the main axis of the collagen fibrils.

Bovine bone femur origins from a 23-month-old female bovine animal from the slaughterhouse Joachim König GmbH (Beelitz, Germany). For storage, samples were frozen at  $-20^\circ\text{C}$  until processing. According to the European directive, no special permit was required for the use of samples from farm animals slaughtered for the food industry using conventional methods and without any other prior treatment.

A human bone femur was obtained from a necropsy sample of a middle-aged woman (52.9 years old) without any known bone-related disease, provided by the Department of Forensic Medicine of the Medical University of Vienna. The donor gave written consent during her lifetime to donate her body to the Center for Anatomy and Cell Biology of the Medical University of Vienna for educational and research purposes. All procedures performed in the study were in accordance with the ethical standards of the ethics committee of the Medical University of Vienna (EK no. 1757/2013).

**High-Pressure Freezing and Freeze Substitution:** Samples were frozen in a Leica HPM 100 (Leica Microsystems) among two  $300 \mu\text{m}$  Type B carriers (Ted Pella Inc.) using 1-hexadecene as cryoprotectant. The vials containing the freeze substitution media (0.1%  $\text{OsO}_4$ , 0.1% uranyl acetate, 0.5% glutaraldehyde, 1.5%  $\text{H}_2\text{O}$  and 100% acetone) were located in the AFS chamber with 100% ethanol. The substitution cycle consists of:  $-120^\circ\text{C}$  for 3h, followed by 2 h warming to  $-85^\circ\text{C}$ , maintaining at  $-85^\circ\text{C}$  for 103h, warming to  $-20^\circ\text{C}$  at a rate of  $7.3^\circ\text{C h}^{-1}$ , maintaining at  $-20^\circ\text{C}$  for 12 h and finally warming to  $4^\circ\text{C}$  at a rate of  $2.6^\circ\text{C h}^{-1}$ . Once at room temperature, samples were extracted from the vials and embedded in Spurr resin (Electron Microscopy Sciences).

**Chemical Fixation:** Samples were fixed in a mixture of 4% acrolein, 2% glutaraldehyde, and 4% paraformaldehyde in 0.12% Cacodylate buffer pH 7.4 for 40 h rinsed  $3 \times 15\text{min}$  in cacodylate buffer, and post-fixed in 1%  $\text{OsO}_4$  in DDW for 3h. After rising  $3 \times 15\text{min}$  in DDW, samples

were dehydrated in acetone series, infiltrated in Spurr resin (Electron Microscopy Sciences) and polymerized at  $65^\circ\text{C}$ .

**Slice-and-View:** Blocks prepared by HPF+FS were polished to expose the tissue and sputter-coated with three layers of carbon ( $\approx 5\text{ nm}$ ) to avoid charging. Serial sectioning (Zeiss Cross-beam 540) was performed at 30 kV FIB acceleration voltage, 100 pA current and slice thickness of 10 nm over an area of  $15 \mu\text{m}^2$  (voxel size  $5 \times 5 \times 10\text{ nm}$ ). Imaging was carried out using a mixed signal of in-lens and BSE detectors (acceleration voltage 1 kV, 57 pA). Image resolution  $1024 \times 768$  pixels, line averaging  $n = 20$ , dwell time 200 ns.

**FIB-SEM Data Processing and 3D Reconstruction:** Brightness/contrast along the dataset was normalized and the stack of images was aligned (registration using Mutual algorithm) and de-noised (Gabor and Vertical de-stripping) using Dragonfly (Object Research Systems, Canada). The image stack was trimmed around the area of interest. Segmentation of the mineral spherulite was performed using the Deep Learning Tool. An input training network based on six carefully manually segmented images was used to train a U-Net, binary model, together with the Adadelta algorithm for optimization. Collagen fibrils segmentation was performed manually, using the contrast thresholding tool.

**Environmental Scanning Electron Microscopy (ESEM):** Resin blocks were initially trimmed with a specimen trimming device (Leica EM TRIM2) and subsequently with a diamond trimming knife (Diatome Trim 45). The block face was cut with an Ultra  $45^\circ$  diamond knife (Diatome) to ensure a flat and even surface. The uncoated block surface was imaged by ESEM (FEI-Thermo Fisher Quanta 600 FEG) at low-vacuum mode (0.75 Torr) and 10 kV acceleration voltage, using the Solid-State Backscattered Electron detector (SSD-BSE).

**Ultramicrotomy:** Ultrathin sections ( $80\text{--}120\text{ nm}$ ) were obtained from chemically fixed samples by ultramicrotomy (Powertome XL, RMC), using an Ultra  $35^\circ$  diamond knife (Diatome). The first cuts were routinely discarded, ensuring fresh, nondamaged surfaces. The slices were floated on ethylene glycol to avoid dissolution of the mineral, and deposited on carbon coated (lacey or continuous foil) Cu grids.

**Fib-Lamellae Preparation by in Situ Lift-Out:** Ultrathin lamellas were prepared by FIB-SEM (Zeiss Cross-beam 540). High pressure frozen and freeze-substituted resin blocks were softly mechanically polished with silicon carbide paper to expose the area of interest and double coated with carbon ( $\approx 5\text{ nm}$ ) to avoid charging. A platinum layer ( $1 \mu\text{m}$ ) was deposited to protect the surface of the sample. Peripheral milling was performed at 30 kV 3 nA, in situ lifted-out and transferred to a Cu 3-Post lift-out grids (Omniprobe) using a micromanipulator (AutoProbe 200, Omniprobe). Thinning was done from both sides of the specimen at  $2^\circ$  incidence angle using a 30 kV ion beam and currents from 50 pA down to 20 pA until the lamella was about 100 nm thick. The final low-kV cleaning was performed at 10 kV, 20 pA, and  $1^\circ$  incidence angle. Electron transparency was checked using the SE2 detector either at 5 or 3kV, resulting in a final thickness of 100 or 60 nm respectively.

**Ion Polished Cross-Sections:** Bone samples were cut with a diamond wired saw in strips ( $3 \times 0.5 \times 0.2\text{ mm}$ , with the longest dimension perpendicular to the long axis of bone), and glued between two silicon wafers. In both, human cortical bone and bovine fibrolamellar bone, the investigated plane was orthogonal to the femur longitudinal axis. Sandwiches were mechanically polished on both sides with silicon carbide paper and diamond lapping foils until  $10\text{--}20 \mu\text{m}$  thickness. Samples were transferred to a molybdenum ring for a final ion milling step using a Precision Ion Polishing System (PIPS 691, Gatan). Thinning to electron transparency was performed by bombarding the sample with argon ions at 4.5 kV while rotating at 3 rpm. Fine thinning was carried out at 2.5 kV, together with a final low-kV cleaning step at 0.5 kV.

**Scanning/Transmission Electron Microscopy (S/TEM):** Measurements were performed in a double Cs corrected Jeol JEM-ARM200F operated at 200 kV. Imaging was performed either in TEM or STEM mode. A combination of detectors (collecting different types of signals) was used to better interpret the material. High Angular Annular Dark Field (HAADF) detector (collection semi-angle  $33\text{--}125\text{ mrad}$ ), Bright Field (BF) detector (collection semi-angle  $15\text{ mrad}$ ), and SE detector were used for imaging.

**STEM-EDS:** Energy Dispersive X-ray Spectroscopy was performed in STEM mode (STEM-EDS) using a windowless Silicon Drift Detector (SSD) with a solid angle of 0.98 steradians and collection area of 100 mm<sup>2</sup> (JEOL). Measurements were carried out at 15 nA emission current, 30 μm diameter C2 aperture, spot size 5C and alpha-tilt angle ( $\alpha = 18^\circ$ ) to reduce x-ray absorption. EDS map from the organic core of the spherulites (Figure 2e) was acquired at 800 kx magnification, covering a total area of 158.4 × 169.7 nm, with 3.8 nm<sup>2</sup> pixel size, exposure time 1 s pixel<sup>-1</sup>, and total exposure time of 31.5 min. EDS map of mineralizing collagen fibrils (Figure 4d) was acquired at 200 kx magnification, covering a total area of 617.9 × 895.5 nm, with 9 nm<sup>2</sup> pixel size, exposure time 1 s pixel<sup>-1</sup>, and total exposure time of 115 min. Individual collagen fibril EDS map (Figure 4j) was acquired at 500 kx magnification, covering a total area of 264.1 × 264.1 nm, with 5 nm<sup>2</sup> pixel size, exposure time 0.7 s pixel<sup>-1</sup>, and total exposure time of 32.77 min. Post-processing of data and standardless quantification was performed using Digital Micrograph v3.0 (Gatan Microscopy Suit).

## Supporting Information

Supporting Information is available from the Wiley Online Library or from the author.

## Acknowledgements

The authors are grateful to Dr. Luca Bertinetti for insightful discussions, and to Dr. Wolfgang Wagermaier for kindly providing the bovine bone specimens. SB gratefully acknowledges financial support from the AUVA (research funds of the Austrian workers' compensation board) and OEGK (Austrian Social Health Insurance Fund).

Open access funding enabled and organized by Projekt DEAL.

## Conflict of Interest

The authors declare no conflict of interest.

## Data Availability Statement

The data that support the findings of this study are available from the corresponding author upon reasonable request.

## Keywords

3D electron microscopy, bone mineralization, collagen mineralization, energy dispersive X-ray spectroscopy, transmission electron microscopy

Received: January 13, 2022

Revised: April 9, 2022

Published online: May 12, 2022

- [1] E. Bonucci, *Front. Biosci. (Landmark Ed)* **2012**, *17*, 100.  
 [2] W. J. Landis, M. Paine, M. J. Glimcher, *J. Ultrastruct. Res.* **1977**, *59*, 1.  
 [3] W. J. Landis, B. T. Hauschka, C. A. Rogerson, M. J. Glimcher, *J. Ultrastruct. Res.* **1977**, *59*, 185.  
 [4] W. J. Landis, M. J. Glimcher, *J. Ultrastruct. Res.* **1978**, *63*, 188.  
 [5] W. Landis, M. Paine, M. J. Glimcher, *J. Ultrastruct. Res.* **1980**, *70*, 171.

- [6] M. D. McKee, A. Nanci, *Cells Mater.* **1993**, *3*, 219.  
 [7] M. D. McKee, A. Nanci, *Microsc. res. techn.* **1995**, *31*, 44.  
 [8] W. J. Landis, M. J. Song, *J. Struct. Biol.* **1991**, *107*, 116.  
 [9] W. J. Landis, K. J. Hodgins, *J. Struct. Biol.* **1996**, *117*, 24.  
 [10] H. S. Gupta, P. Roschger, I. Zizak, N. Fratzl-Zelman, A. Nader, K. Klaushofer, P. Fratzl, *Calcif. Tissue Int.* **2003**, *72*, 567.  
 [11] E. M. Spiesz, P. Roschger, P. K. Zysset, *Calcif. Tissue Int.* **2015**, *90*, 319.  
 [12] Z. Zou, T. Tang, E. Macías-Sánchez, L. Bertinetti, W. J. Landis, P. Fratzl, *Proc. Natl. Acad. Sci. U.S.A.* **2020**, *117*, 14102.  
 [13] M. Ayoubi, A. F. van Tol, R. Weinkamer, P. Roschger, P. C. Brugger, A. Berzlanovich, L. Bertinetti, A. Roschger, P. Fratzl, *Adv. Healthcare Mater.* **2021**, *10*, 2100113.  
 [14] F. A. Shah, K. Ruscsák, A. Palmquist, *Bone Rep.* **2020**, *13*, 100283.  
 [15] D. Buss, N. Reznikov, M. McKee, *J. Struct. Biol.* **2020**, *212*, 107603.  
 [16] V. Jantou-Morris, M. A. Horton, D. W. McComb, *Biomaterials* **2010**, *31*, 5275.  
 [17] E. McNally, H. P. Schwarcz, G. A. Botton, A. L. Arsenault, *PLoS One* **2012**, *7*, e29258.  
 [18] N. Reznikov, M. Bilton, L. Lari, M. M. Stevens, R. Kröger, *Science* **2018**, *360*, eaao2189.  
 [19] M. J. Olszta, X. Cheng, S. S. Jee, R. Kumar, Y.-Y. Kim, M. J. Kaufman, E. P. Douglas, L. B. Gower, *Mater. Sci. Eng. R* **2007**, *58*, 77.  
 [20] A. Farzadi, T. Renner, E. P. Calomeni, K. F. Presley, N. Karn, J. Lannutti, L. P. Dasi, G. Agarwal, *Mater. Sci. Eng. C* **2019**, *104*, 109905.  
 [21] D. J. McBride, R. A. Hahn, F. H. Silver, *Int. J. Biol. Macromol.* **1985**, *7*, 71.  
 [22] L. Chen, R. Jacquet, E. Lowder, W. J. Landis, *Bone* **2015**, *71*, 7.  
 [23] A. Shtukenberg, Y. O. Punin, E. Gunn, B. Kahr Spherulites, *Chem. Rev.* **2012**, *112*, 1805.  
 [24] L. Gránásy, T. Pusztai, G. Tegze, J. A. Warren, J. F. Douglas, *Phys. Rev. E* **2005**, *72*, 011605.  
 [25] F. F. Amos, L. Dai, R. Kumar, S. R. Khan, L. B. Gower, *Urol. Res.* **2009**, *37*, 11.  
 [26] H. Tlatlik, P. Simon, A. Kawska, D. Zahn, R. Kniep, *Angew. Chem., Int. Ed.* **2006**, *45*, 1905.  
 [27] S. Elsharkawy, M. Al-Jawad, M. F. Pantano, E. Tejada-Montes, K. Mehta, H. Jamal, S. Agarwal, K. Shuturminska, A. Rice, N. V. Tarakina, R. M. Wilson, A. J. Bushby, M. Alonso, J. C. Rodriguez-Cabello, E. Barbieri, A. del Río Hernández, M. M. Stevens, N. M. Pugno, P. Anderson, A. Mata, *Nat. Commun.* **2018**, *9*, 2145.  
 [28] D. J. Lipomi, R. V. Martinez, R. M. Rioux, L. Cademartiri, W. F. Reus, G. M. Whitesides, *CS Appl. Mater. Interfaces* **2010**, *2*, 2503.  
 [29] J. C. Jesior, *J. Ultrastruct. Mol. Struct. Res.* **1986**, *95*, 210.  
 [30] P. Fratzl, M. Groschner, G. Vogl, H. Plenck, J. Eschbergerr, N. Fratzl-Zelman, K. Koller, K. Klaushofer, *J. Bone Miner. Res.* **1992**, *7*, 329.  
 [31] D. F. Holmes, C. J. Gilpin, C. Baldock, U. Ziese, A. J. Koster, K. E. Kadler, *Proc. Natl. Acad. Sci. U.S.A.* **2001**, *98*, 7307.  
 [32] J. P. R. O. Orgel, T. C. Irving, A. Miller, T. J. Wess, *Proc. Natl. Acad. Sci. U.S.A.* **2006**, *103*, 9001.  
 [33] H. P. Schwarcz, E. A. McNally, G. A. Botton, *J. Struct. Biol.* **2014**, *188*, 240.  
 [34] K. Grandfield, V. Vuong, H. P. Schwarcz, *Calcif. Tissue Int.* **2018**, *103*, 606.  
 [35] B. E. J. Lee, L. Luo, K. Grandfield, C. M. Andrei, H. P. Schwarcz, *Micron* **2019**, *124*, 102706.  
 [36] B. Boothroyd, *Clin. Orthop. Relat. Res.* **1975**, *106*, 290.  
 [37] D. D. Lee, M. J. Glimcher, *J. Mol. Biol.* **1991**, *217*, 487.  
 [38] W. J. Landis, M. J. Song, T. A. Leith, L. McEwen, B. F. McEwen, *J. Struct. Biol.* **1993**, *110*, 39.  
 [39] D. Torioian, J. E. Lim, P. A. Price, *J. Biol. Chem.* **2007**, *282*, 22437.  
 [40] P. Bianco, Y. Hayashi, G. Silvestrini, J. D. Termine, E. Bonucci, *Calcif. Tissue Int.* **1985**, *37*, 684.

- [41] H. S. Gupta, J. Seto, W. Wagermaier, P. Zaslansky, P. Boesecke, P. Fratzl, *Proc. Natl. Acad. Sci. U.S.A.* **2006**, *103*, 17741.
- [42] B. A. Cressey, G. Cressey, *Mineral. Mag.* **2003**, *67*, 1171.
- [43] M. A. Rubin, I. Jasiuk, J. Taylor, J. Rubin, T. Ganey, R. P. Apkarian, *Bone* **2003**, *33*, 270.
- [44] K. Hoshi, S. Ejiri, W. Probst, V. Seybold, T. Kamino, T. Yaguchi, N. Yamahira, H. Ozawa, *J. Microscopy* **2000**, *201*, 44.
- [45] P. Bianco, M. Riminucci, G. Silvestrini, E. Bonucci, J. D. Termine, L. W. Fisher, P. G. Robey, *J. Histochem. Cytochem* **1993**, *41*, 193.
- [46] H. Nakamura, A. Hirata, T. Tsuji, T. Yamamoto, *Arch. Histol. Cytol.* **2001**, *64*, 109.
- [47] E. S. Hara, M. Okada, N. Nagaoka, T. Hattori, T. Kuboki, T. Nakano, T. Matsumoto, *ACS Biomater. Sci. Eng.* **2018**, *4*, 617.
- [48] Y. Xu, F. Nudelman, E. D. Eren, M. J. M. Wirix, B. Cantaert, W. H. Nijhuis, D. Hermida-Merino, G. Portale, P. H. H. Bomans, C. Ottmann, H. Friedrich, W. Bras, A. Akiva, J. P. R. O. Orgel, F. C. Meldrum, N. Sommerdijk, *Nat. Commun* **2020**, *11*, 5068.
- [49] S. Weiner, W. Traub, *FEBS Lett.* **1986**, *206*, 262.